




Fabrication of perovskite solar cells in ambient air by blocking perovskite hydration with guanabenz acetate salt

Received: 13 September 2022

Accepted: 22 August 2023

Published online: 28 September 2023

 Check for updates

Luyao Yan^{1,2}, Hao Huang^{1,2}, Peng Cui^{1,2} , Shuxian Du¹, Zhineng Lan¹, Yingying Yang¹, Shujie Qu¹, Xinxin Wang¹, Qiang Zhang¹, Benyu Liu¹, Xiaopeng Yue¹, Xing Zhao¹, Yingfeng Li¹, Haifang Li¹, Jun Ji¹ & Meicheng Li¹  

The fabrication of perovskite solar cells (PSCs) in ambient air can accelerate their industrialization. However, moisture induces severe decomposition of the perovskite layer, limiting the device efficiency. Here we show that sites near vacancy defects absorb water molecules and trigger the hydration of the perovskite, eventually leading to the degradation of the material. We demonstrate that guanabenz acetate salt eliminates both cation and anion vacancies, blocking the perovskite hydration and allowing the crystallization of a high-quality film in ambient air. With guanabenz acetate salt, we prepare PSCs in ambient air with a certified efficiency of 25.08%. The PSCs without encapsulation maintain around 96% of their initial efficiency after 2,000 hours of ageing in ambient air and after 500 hours of operating at the maximum power point under simulated air mass (AM) 1.5 G solar light in a N₂ atmosphere. The encapsulated devices retained 85% of their initial efficiency after 300 hours under damp heat conditions (85 °C and 85% relative humidity).

Metal halide perovskite solar cells (PSCs) have attracted much research attention as a tremendous potential photovoltaic technology, with their power conversion efficiency (PCE) now exceeding 25.8% (refs. 1,2). Massive efforts—crystallization regulation, defect passivation and interface and structure design—have been devoted to improving the efficiency and stability of PSCs^{3–11}. However, the fabrication of these >25% efficient and stable PSCs requires an inert atmosphere (for example, nitrogen glovebox)^{12–14}, which restricts their large-scale production and practical applications. Therefore, the fabrication of high-performance PSCs in ambient air is expected to promote their practical applications and low-cost commercialization.

Unfortunately, lead halide perovskite is extremely sensitive to moisture in ambient air, which can lead to initial hydration, followed by disruptive phase transitions, destruction of the crystal framework and decomposition^{15–20}. Hence, the fabrication of highly efficient PSCs is strictly limited to a glovebox; thus, it is difficult to fabricate

them in a scaled and industrialized fashion. The space expansion of a glovebox is intractable from technical and economic perspectives. In an effort to obtain high-efficiency PSCs independent of the inert atmosphere, researchers have adapted the fabrication of PSCs to various environmental conditions^{21–32}. The additive strategy^{25,26} is a valid approach to optimizing perovskite crystallization and preventing moisture vulnerability in ambient air, such as 19.4% efficient PSCs enabled via PbS quantum dots at 40–60% relative humidity (RH)²⁶. Antisolvent engineering and environmental condition control in the deposition process can also reduce the moisture impacts and accelerate perovskite crystallization, promoting PSCs with efficiencies exceeding 22% at 50–70% RH^{27–30}. Remarkably, the use of ionic liquids^{4,31,32} is proposed to obtain stable perovskite in ambient air; the ionic liquids induce vertical lead iodide to achieve a fast transformation to stable α -FAPbI₃ and can produce PSCs with an efficiency of 24.1% at 80% RH⁴. However, an approach to truly throw off the impact

¹State Key Laboratory of Alternate Electrical Power System with Renewable Energy Sources, School of New Energy, North China Electric Power University, Beijing, China. ²These authors contributed equally: Luyao Yan, Hao Huang, Peng Cui. ✉ e-mail: mcli@ncepu.edu.cn

of moisture on the fabrication of PSCs to obtain an efficiency of over 25% in ambient air is lacking.

We aim to design a strategy that focuses on the first stage of perovskite hydration to protect the perovskite from water. Hydration is generated more easily near the vacancy sites located on the perovskite surface and grain boundary, which can drastically accelerate the moisture-induced decomposition of perovskite films^{33,34}. Hence, eliminating the vacancies is a feasible approach to decreasing the perovskite sensitivity to water. The cation vacancies can be effectively filled by an organic group, which possesses suitable charges and a similar molecular size to formamidinium ions (FA⁺)^{35,36}. In addition, pseudohalide anions with strong electronegativities, such as HCOO⁻ and CH₃COO⁻, cannot only suppress anion-vacancy defects but also augment the crystallinity of films¹⁴. On the basis of the above analysis, guanabenz acetate salt (GBA) should be a suitable material; its structure includes acetate (AC⁻) and guanidine groups, which theoretically can suppress both cation and anion vacancies and synergistically optimize crystallization. GBA also includes a benzene ring that possesses a high electron cloud density to passivate perovskite neutral defects and a concrete molecular structure to maintain the guanidine group anchoring on the perovskite surface and grain boundary³⁷.

Here we report highly efficient PSCs fabricated fully in ambient air by blocking the hydration pathway of perovskite at the source using GBA. GBA significantly eliminates the vacancy and increases the binding energy of perovskite with H₂O, removing the detrimental interference of moisture on perovskite crystallization. The resulting PSCs obtained an efficiency of 25.32% (certified 25.08%) with an aperture area of 0.08 cm² and maintained 97% of the initial PCE after 2,000 hours of ageing in ambient air without encapsulation. The unencapsulated PSCs retained 96% of the initial PCE after maximum power point (MPP) tracking under continuous illumination (~50 °C) in N₂ atmosphere for 500 hours. Moreover, the encapsulated PSCs exhibited excellent stability under damp heat tests (85 °C and 85% RH). These PSCs retained 85% of their original PCE values after 300 hours of testing at 85% RH.

Characterization of perovskite films fabricated in air

We deposited perovskite films in various humid atmospheres, and distinctive phenomena in structural and photoelectric properties with and without GBA (Supplementary Fig. 1 shows the chemical structure) were demonstrated. The quality of control perovskite films containing no GBA becomes very poor without inert atmosphere protection; this finding was confirmed by the morphology and crystallinity results (via scanning electron microscopy (SEM) and grazing incidence wide-angle X-ray scattering (GIXRD)). In the control film, the number of pinholes and PbI₂ on the surface increases with increasing humidity (Fig. 1a and Supplementary Fig. 2), which is consistent with previous reports²². Figure 1b,c shows the 2D GIXRD ring patterns and the corresponding 1D integral spectra of the control films, respectively. When the deposition of perovskite films is exposed to moisture, the signal of the wide-bandgap yellow phase (δ -FAPbI₃) begins to be captured, and the integrated intensity of the α -FAPbI₃ peak located near 14° decreases. Additionally, the increase in humidity causes a shift of the peak in the 1D integral spectra, which indicates that the perovskite structure distortion is impacted by moisture. These undesirable structural deviations are worsened with increasing humidity, suggesting the adverse impacts of moisture on the crystallinity of perovskite, which impedes the formation of ideal α -FAPbI₃ and induces composition segregation^{14,18}.

In contrast to the control films, the target films exhibit excellent quality even when their deposition process is exposed to moisture (incorporated 3% GBA). Their surface morphology shows no evident difference with increasing humidity (Fig. 1d). The film deposited under ~80% RH (~20 °C) in ambient air still possesses a pinhole-free and dense characteristic. In Fig. 1e,f, the integrated intensity of the α -FAPbI₃ peak can maintain a remarkable consistency under different humidities, and

distortion of the perovskite structure was prevented. The formation of δ -FAPbI₃ is completely inhibited by incorporating GBA, even in ambient humidity as high as 80% RH. In addition, the intensity of the PbI₂ peak in the target perovskite XRD image is decreased compared with that of the control film (Supplementary Fig. 3 and Supplementary Note 1). These ideal film properties confirm that GBA can protect crystallization from moisture in ambient air, resulting in compact and α -FAPbI₃-preferred perovskite films.

We also evaluated the photoelectric property differences of perovskite films deposited in ambient air in terms of spatial uniformity and photoluminescence spectroscopy. Notably, the following control and target samples were prepared in ambient air under ~55% RH (~20 °C) unless specified. Kelvin probe force microscopy (KPFM) measurements were carried out to examine the surface potential of the films (Fig. 2a,b and Supplementary Fig. 4). The target film exhibits a higher potential than the control film, which could be attributed to the decreased surface electronic trap density³⁸. The increase in surface potential is consistent with the ultraviolet photoelectron spectrometer results (Supplementary Figs. 5 and 6 and Supplementary Note 2). Additionally, the potential distribution of the target film is ~33 mV, which is smaller than that of the control film (~48 mV). From the photoluminescence (PL) images of both films, the target film clearly exhibits an enhanced PL intensity compared to that of the control film (Fig. 2c,d and Supplementary Fig. 7). Specifically, the PL intensity distribution in the target film is more spatially uniform than that in the control film, which is consistent with the KPFM results. The uniform distribution of potential and PL intensity indicates that the incorporated GBA improves the quality of perovskite films.

The photoluminescence quantum efficiency (PLQE) was measured to quantitatively evaluate the luminous efficiencies of both films deposited in ambient air (Fig. 2e). The PLQE of the control film is 3.64 ± 2.14%, while the target film exhibits a significantly increased PLQE of 17.90 ± 1.49%, demonstrating its superior radiative ability after incorporating GBA. The carrier lifetime from time-resolved photoluminescence (TRPL) of the target film is prolonged from 0.77 μ s to 2.26 μ s (Fig. 2f), indicating fewer trap states. In short, these remarkable structural and photoelectric phenomena verify that the incorporated GBA can decrease the sensitivity of perovskite crystallization to moisture, ensuring the formation of a high-quality perovskite film deposited in ambient air.

To visually observe the decreased moisture sensitivity of the target film, water-soaking tests were conducted. The decomposition process under continuous spray soaking of perovskite films was observed in situ under an optical microscope (Fig. 2g). The control and target films show an apparent decomposition difference in the time response. The control film degrades immediately under spray soaking, while the target film can maintain stability for up to 24 s, suggesting the moisture insensitivity resulting from the use of GBA. Additionally, harsher water dropping and immersing tests were carried out (Supplementary Figs. 8 and 9). When contacting the water, the control film shows a colour change from black to yellow within 3 s, while the target film can maintain the black colour for over 15 s, which is consistent with the results from the spray soaking tests. Subsequently, we performed a contact angle test, and the results showed that the control and target films had similar water drop contact angles (Supplementary Fig. 10). According to the contact angle tests, the reason for decreased moisture sensitivity of the target film is not supposed to be forming a hydrophobic surface. Considering the improved photoelectric property of the target film, we speculate that the decreased moisture sensitivity may be closely relevant to the eliminated vacancy that is reported to mainly exist in the grain boundary and surface^{39,40} (Supplementary Figs. 11 and 12 and Supplementary Note 3).

Confirmation of hydration blocking

The reason for the high-quality perovskite film achieved in ambient air was examined; GBA blocks the hydration pathway, that is, the initial

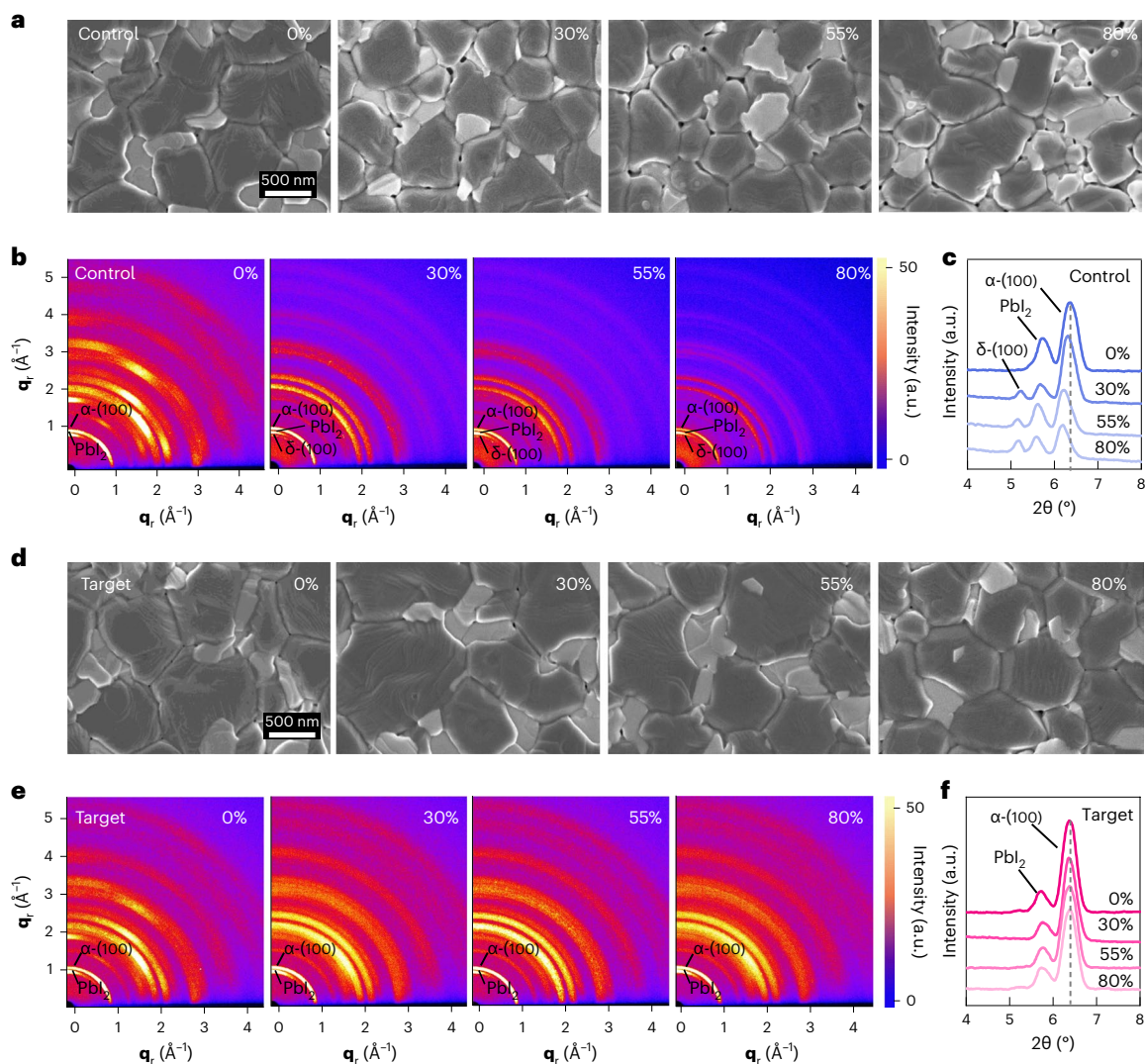


Fig. 1 Morphology and crystallinity characterization of perovskite films.

a–f, Both control and target films are fabricated under different humidities (0–80% RH). **a**, SEM images of control films. **b**, 2D GIXRD ring patterns of control films. q_r is the scattering vector. **c**, 1D GIXRD integral spectra of control films.

d, SEM images of target films. **e**, 2D GIXRD ring patterns of target films. **f**, 1D GIXRD integral spectra of target films. The vertical dashed lines in **c** and **f** are the position of α -(100) phase.

interaction stage between moisture and perovskite. Initially, the mechanism of moisture-induced decomposition was analysed (Fig. 3a, left). An atom exposed by a vacancy in perovskite can bind with H_2O molecules more easily in energetics^{16,33,34,39,40}, which is the beginning of the hydration process. The subsequent process induces the escape of the FAI and collapse of the PbI_2 framework^{19,41}. To investigate the dominant impact of vacancies on hydration, density functional theory (DFT) studies were carried out to calculate the binding energy of H_2O molecules with the perovskite (Fig. 3b and Supplementary Table 1). Γ and FA^+ vacancies are readily formed during film deposition¹⁵. When there is a FA^+ vacancy in the structure (Supplementary Fig. 13), the binding energies of H_2O molecules with FA^+ , Pb^{2+} and Γ are -1.134 eV, -1.133 eV and -1.461 eV, respectively. When there is an Γ vacancy (Supplementary Fig. 14), the binding energies of H_2O with FA^+ , Pb^{2+} and Γ are -1.450 eV, -0.610 eV and -1.189 eV, respectively. Conversely, in an ideal perovskite structure (Supplementary Fig. 15), the binding energies of H_2O molecules with FA^+ , Pb^{2+} and Γ are 1.020 eV, 1.446 eV and 1.774 eV, respectively. These results indicate that H_2O molecules can be favourably absorbed near vacancy sites and induce perovskite decomposition, which suggests that eliminating vacancies is a feasible approach to decreasing the sensitivity of perovskites to moisture.

GBA can eliminate vacancies through interaction with perovskite (Fig. 3a, right). GBA is an aromatic amine salt, including AC^- , which possesses strong coordination ability, and a terminated guanidine group in the benzene ring, which forms a greater number of effective hydrogen bonds than FA^+ ⁴². From the Fourier transform infrared (FTIR) spectra of GBA and the target film (Fig. 3c), both the corresponding absorption peaks of $C=O$ and $C-O$ of GBA shift to a lower wavenumber after being incorporated into the perovskite film, implying that an interaction occurred between GBA and perovskite⁴³. Specifically, the evident downshift of $Pb\ 4f$ core levels in the target film also confirms the above interaction (X-ray photoelectron spectroscopy; Fig. 3d, Supplementary Fig. 16 and Supplementary Note 4), indicating that GBA can fill the Γ vacancy through binding with the unsaturated Pb^{2+} ⁴⁴. Additionally, the smaller binding energy of $Pb^{2+}-AC^-$ demonstrates that the unsaturated Pb^{2+} will preferentially connect with AC^- through a stronger $Pb-O$ bond rather than the H_2O molecule upon comparison of the binding energies of $Pb^{2+}-AC^-$ (-2.401 eV) and $Pb^{2+}-H_2O$ (-0.610 eV) when Γ vacancies are present (Supplementary Fig. 17 and Supplementary Table 2).

Additionally, it was speculated that the FA^+ vacancy was filled by the terminated guanidine group of GBA based on the formed hydrogen

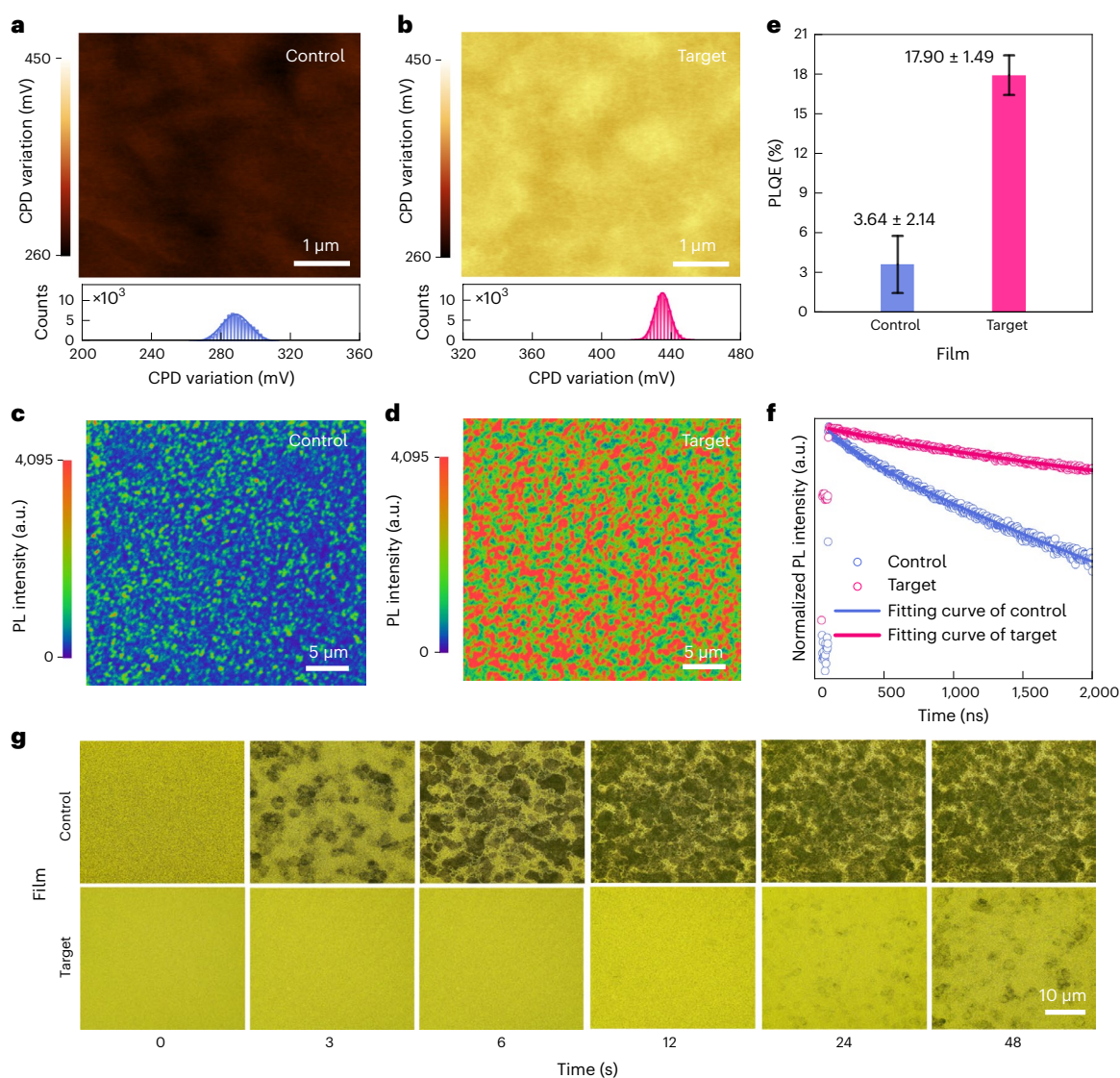


Fig. 2 | Photoelectric property characterization of perovskite films.

a, b, Surface potential images of control (**a**) and target (**b**) films. The statistical potential distributions of film surfaces are shown at the bottom. CPD, contact potential difference. **c, d**, PL mapping of control (**c**) and target (**d**) films. **e**, PLOE results of control and target films (five samples for each). The height of the box

represents the average value, and the upper and lower boundaries of the error bar represent the maximum and minimum values respectively. **f**, TRPL spectra of control and target films. **g**, In situ optical microscopy images of morphology evolution under continuous water spray of control and target perovskite films.

bond and energetic stability calculation. The $I\ 3d$ core levels of the target film exhibited a downshift (Supplementary Fig. 18), implying the Γ vacancy was filled by AC^- and the formation of a hydrogen bond between the terminated guanidine group of GBA and the I atom⁴¹. In addition, the terminated guanidine group of GBA interacted with the PbI_2 film substrate through a hydrogen bond, which was also confirmed by the shift of $C = N$ in the PbI_2 film-incorporated GBA (Supplementary Fig. 19)³⁵. From the view of energetics, after the terminated guanidine filled the FA^+ vacancy, the DFT calculation showed that Γ^- vacancy formation was suppressed by 0.28 eV (Supplementary Fig. 20 and Supplementary Note 5), resulting in a stable perovskite lattice³³.

To verify that the incorporated GBA eliminates both Γ^- and FA^+ vacancies in perovskite, we carried out deep energy level transient spectroscopy (DLTS) measurements (Fig. 3e). The DLTS signals of the control film exhibited two peaks marked with T1 and T2, indicating two types of dominant traps. The Arrhenius plots were fitted (Fig. 3f) to calculate the activation energy of the corresponding traps according to the following Arrhenius equation:

$$\ln(t_{\text{au}} \times V_{\text{th}} \times N_c) = \frac{E_T - E_V}{KT} - \ln(X_p \sigma_p)$$

where K is the Boltzmann constant, t_{au} is the emission time constant, V_{th} is the thermal velocity, N_c is the effective density of states of the trap in cm^{-3} , X_p is the entropy factor and σ_p is the capture cross section, T is the temperature of test, E_T is the energy level of the trap center and E_V is the energy level of VBM. The trap activation energy ($\Delta E = E_T - E_V$) of T1 was calculated to be 0.51 eV and that of T2 was calculated to be 0.39 eV, which represent the FA^+ vacancy and Γ^- vacancy in the control film, respectively^{45,46}. Remarkably, the DLTS signals of the target film did not exhibit any trap peaks, indicating that the incorporated GBA effectively eliminated the vacancy. The decreased trap density resulting from the GBA was also confirmed by the space-charge-limited current (SCLC) measurements (Supplementary Figs. 21 and 22 and Supplementary Note 6). In addition, we calculated the carrier mobility and diffusion length of the control and target films. The results showed that the carrier mobility and diffusion length of the target films increased from

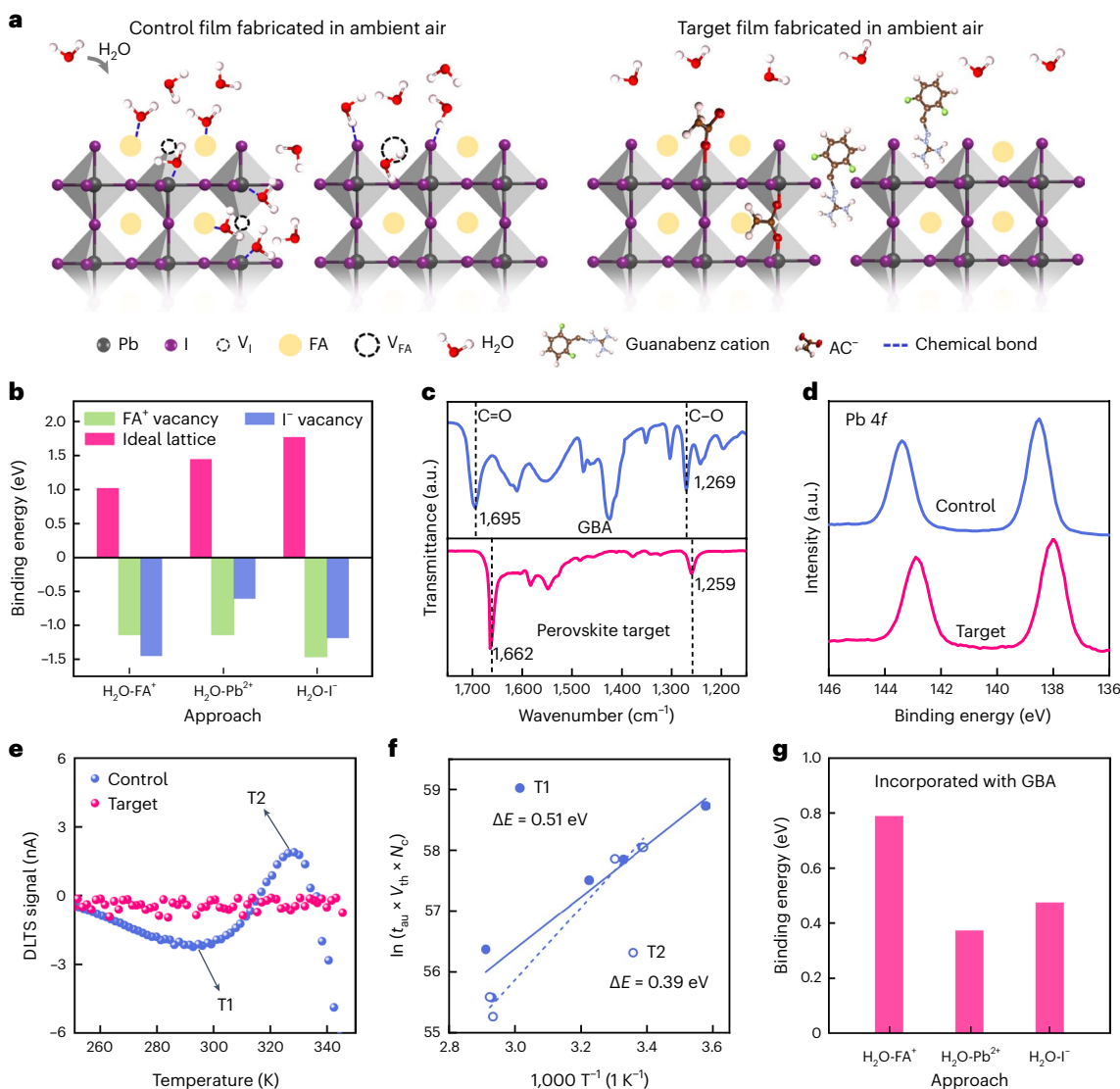


Fig. 3 | Characterization of the interaction between perovskite and GBA.

a, Schematic illustration of the moisture-induced decomposition and the decreased moisture sensitivity caused by the addition of GBA. **b**, The binding energies of H₂O molecules with perovskite through H₂O-FA⁺, H₂O-Pb²⁺ and H₂O-I⁻ approaches when the structure contained FA⁺ vacancies, I⁻ vacancies and no vacancies. **c**, FTIR spectra of GBA and the target film. **d**, XPS characterization of Pb in the control and target films. The vertical dashed line is the position of C = O

and C–O chemical bond. **e, f**, Deep energy level transient spectroscopy (DLTS) spectra of control and target films. **(e)** and corresponding Arrhenius plots **(f)** with fitting. The data points in **f** are obtained by calculating internal transients that are included in the DLTS signals using the discrete Laplace transform, and the lines are linear fits of the data points. **g**, The binding energies of H₂O molecules with the perovskite through H₂O-FA⁺, H₂O-Pb²⁺ and H₂O-I⁻ approaches when the structure incorporated GBA.

1.98 cm² V⁻¹ s⁻¹ and 1.96 μm to 2.68 cm² V⁻¹ s⁻¹ and 3.92 μm, respectively (Supplementary Table 3 and Supplementary Note 7).

The effects of the decreased moisture sensitivity of perovskite due to the elimination of vacancies by GBA were investigated. On the basis of the I⁻ vacancy and FA⁺ vacancy filled by the AC⁻ and terminated guanidine groups of GBA, respectively, we calculated the binding energies of H₂O molecules with FA⁺, Pb²⁺ and I⁻ to be 0.790 eV, 0.373 eV and 0.475 eV, respectively (Fig. 3g, Supplementary Fig. 23 and Supplementary Table 1). After incorporating GBA, the binding energy of H₂O molecules with the perovskite transformed from negative (Fig. 3b) to positive (Fig. 3g), implying harder to bind. The positive value would indicate that the interaction of H₂O molecules with the perovskite was not spontaneous or immediate. Hence, the intercepted perovskite hydration by GBA could effectively protect the perovskite crystallization from moisture, ensuring the deposition of high-quality perovskite films for fabricating efficient PSCs in ambient air (Fig. 3a).

Performance of PSCs fabricated in ambient air

We utilized high-quality perovskite films that incorporated GBA further to fabricate PSCs (FTO/c-TiO₂/FA_{0.98}MA_{0.02}PbI₃/o-F-PEAI/Spiro-OMeTAD/Au) in ambient air. After exploring the influence of the GBA concentration on the PCE of PSCs (Supplementary Fig. 24 and Supplementary Table 4), we determined that the optimal concentration was 0.045 M (the molar ratio of GBA/PbI₂ is 3%). Figure 4a displays the current density–voltage (*J*–*V*) curves (reverse) of the champion control and target PSCs, in which the aperture area is 0.08 cm². The target PSCs reach a PCE of 25.32% with low hysteresis, while the PCE of the control PSCs is 23.13% (Supplementary Fig. 25 and Supplementary Table 5). Specifically, the target PSCs exhibit an open voltage (*V*_{oc}) of 1.174 V, which is much higher than that (1.141 V) of control PSCs. The stabilized PCE of the target PSCs is 25.03%, measured at the maximum power point (Supplementary Fig. 25). The corresponding external quantum efficiency (EQE) spectra of the control and target PSCs are shown in Fig. 4b, in

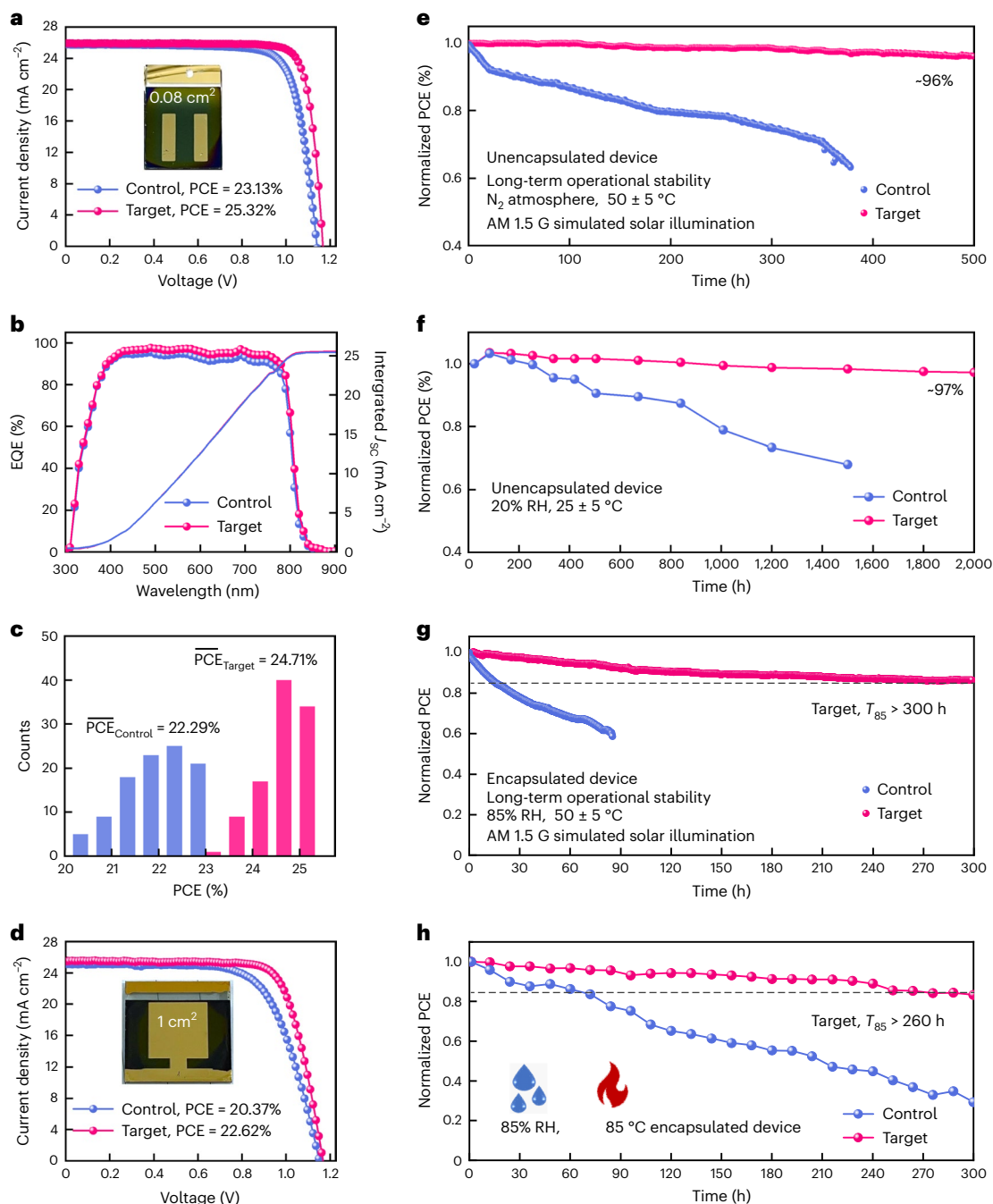


Fig. 4 | Photovoltaic performance of control and target PSCs. a, J - V curves of the champion control and target PSCs with an aperture area of 0.08 cm^2 . Inset, a photograph of the PSC. **b**, EQE spectra of control and target PSCs. **c**, Histogram of the PCE value among 100 PSCs. **d**, J - V curves of the champion control and target PSCs with an aperture area of 1 cm^2 . **e, f**, Normalized PCE of the unencapsulated control and target PSCs measured at MPP under continuous 1 sun illumination

in N_2 atmosphere (**e**) and stored in ambient air at 20% RH and $25 \pm 5^\circ \text{C}$ in the dark (**f**). **g, h**, Normalized PCE of the encapsulated control and target PSCs measured at MPP under continuous 1 sun illumination at 85% RH (**g**) and stored at 85°C and 85% RH in the dark (**h**). The horizontal dashed line is the 85% of initial PCE. The initial photovoltaic parameters of the control and target PSCs in the stability test were listed in Supplementary Table 9.

which the value of integrated short-circuit current density (J_{sc}) is basically consistent with that obtained from the J - V curves. The target PSCs also possess satisfactory reproducibility with an average PCE of 24.71% (Fig. 4c and Supplementary Fig. 26). One of the best performing target PSCs was certified by an independent solar cell-accredited laboratory (National Institute of Metrology, China) and achieved a PCE of 25.08% (Supplementary Fig. 27). We directly compared reported PSCs fabricated fully in ambient air with those in our work (Supplementary Fig. 28 and Supplementary Table 6) and showed that the PCE of 25.32%

obtained in our work significantly promoted the advances of ambient air-fabricated PSCs.

The incorporated GBA ensures a uniform perovskite film deposited in ambient air, which is further used to fabricate PSCs with an aperture area of 1 cm^2 (Fig. 4d). On the basis of the same composition and device structure, the control PSCs exhibit a PCE of 20.37%, with a J_{sc} of 25.20 mA cm^{-2} , a V_{oc} of 1.148 V and a fill factor of 71.23%. In contrast, the PCE of the target PSCs improved to 22.62%, with a J_{sc} of 25.43 mA cm^{-2} , a V_{oc} of 1.161 V and the fill factor increased to 76.60% (Supplementary

Fig. 29 and Supplementary Table 7). The effectively improved performance in large-area PSCs indicates the further potential of our work in scalable industrialization.

It has been reported that there are various types and amounts of defect in different perovskite components^{47,48}. To verify the expandability of GBA in improving the performance of other perovskites, we also fabricated PSCs (FTO/c-TiO₂/MA_{0.75}FA_{0.25}PbI₃/o-F-PEAI/Spiro-OMeTAD/Au, the aperture area is 0.08 cm²) by the one-step method in ambient air. The target PSCs exhibit a PCE of 23.71%, which is higher than that (22.22%) of the control PSCs (Supplementary Fig. 30, Supplementary Note 8 and Supplementary Table 8). In detail, the J_{sc} of the target PSCs is 24.83 mA cm⁻², which shows a small variation with the integrated J_{sc} of the corresponding EQE measurement.

To investigate the effect of incorporated GBA on PSCs' intrinsic stability, the PCE evolution of unencapsulated PSCs under various conditions was monitored. We examined the long-term operational stability through MPP tracking of the unencapsulated PSCs under continuous AM 1.5 G (100 mW cm⁻²) solar light in a N₂ atmosphere at 50 ± 5 °C (Fig. 4e). The target PSCs could maintain 96% of their initial PCE after 500 hours. Conversely, the control PSCs dropped to <65% of the initial PCE in no more than 400 hours. GBA enhanced the operational stability of the PSCs due to the eliminated vacancy that was beneficial for ion migration, based on the reported degradation mechanism of PSCs during operation⁴⁶. We further monitored the PCE evolution of unencapsulated PSCs stored in ambient air. The PCE of the target PSCs showed no evident decline after 2,000 hours of ageing, while the PCE of the control PSCs maintained only 68% of the initial value (Fig. 4f). The enhanced air stability of the target PSCs could be ascribed to the decreased sensitivity of the perovskite film to moisture.

The extrinsic stability of PSCs was also assessed following the International Summit on Organic Photovoltaic Stability standardized stability testing procedure⁴⁹. Initially, we performed MPP tracking of the encapsulated PSCs under continuous AM1.5 G (100 mW cm⁻²) solar light in ambient air at 85% RH. As shown in Fig. 4g, the target PSCs maintained 85% of their initial PCE after 300 hours of operation at 85% RH. In contrast, the control PSCs dropped to <60% of the initial PCE in no more than 90 h. Then, we conducted stricter stability measurements on the encapsulated PSCs, as shown in Fig. 4h. The target PSCs exhibited T85 > 260 hours under the damp heat test (85 °C and 85% RH), while the control PSCs showed rapid decay. We also performed the accelerated degradation measurements of unencapsulated PSCs stored at 65% RH; the target PSCs show better moisture stability than control PSCs (Supplementary Fig. 31). On the basis of these results, GBA ensured the excellent stability of PSCs fabricated in ambient air, which enabled high-performance PSC fabrication that no longer required an inert atmosphere; this process could quickly lead towards the commercialization of these PSCs.

Discussion

In summary, high-efficiency PSCs were completely fabricated in ambient air by blocking hydration. On the basis of the critical role of the vacancy on perovskite hydration, perovskite crystallization was protected from moisture by eliminating the vacancy sites through the incorporation of GBA, ensuring the formation of high-quality perovskite films in ambient air. Due to the finely controlled perovskite crystallinity and decreased vacancy trap states, the PSCs fabricated in ambient air obtained a PCE of 25.32% (certified 25.08%); this is the highest value among the PSCs fabricated in the open environment up to date and rivals the state-of-the-art PSCs fabricated in a glovebox. In addition, unencapsulated PSCs exhibit excellent long-term stability, which can maintain 96% of their initial efficiency after 500 hours of operating at the maximum power point under simulated AM 1.5 G solar light. This work provides a feasible approach to enable high-performance PSC fabrication that no longer required an inert atmosphere and can quickly lead toward the commercialization of these efficient PSCs.

Methods

Materials

The materials consisted of the following: FTO glass substrate (12–14 ohm); TiCl₄ (Aladdin, 99.9%); lead iodide (Sigma-Aldrich, 99.9%); guanabenz acetate salt (Aladdin); DMF (Sigma-Aldrich); DMSO (Sigma-Aldrich); isopropanol (Acros, 99.8%); chlorobenzene (Sigma-Aldrich, 99.5%); acetonitrile (Acros, 99.9%); FAI, MAI, MACI, o-F-PEAI, Spiro-OMeTAD, lithium bis(trifluoromethanesulfonimide) and 4-tert-butylpyridine (Xi'an Polymer Light Technology Corp).

Device fabrication in ambient air

Preparation of the FTO glass substrate: the FTO glass substrate was ultrasonically cleaned with deionized water, ethanol and deionized water for 15 min each. After drying the substrate with a high-purity N₂ stream, the substrate was treated with ultraviolet ozone for 15 min to obtain the hydrophilic surface.

Preparation of the compact TiO₂ electron transport layer: to prepare the TiO₂ electron transport layers, TiCl₄ (3 ml) and deionized water (200 ml) were mixed and stirred to obtain a TiO₂ precursor. Then the FTO substrate was immersed into the precursor and stored in a water bath at 70 °C for 40 min to obtain the compact TiO₂ layer. Before spin coating the perovskite precursor, the FTO/TiO₂ substrate was treated with UV-ozone for 15 min to improve infiltration and passivate oxygen vacancy defect⁵⁰.

Preparation of perovskite via the two-step method with different humidities: a 1.5 M PbI₂ (DMF: DMSO, 9:1 volume/volume) precursor with different ratios of guanabenz acetate (GBA, the molar ratio of GBA/PbI₂ was 1%, 3%, 5%) was spin coated on the FTO/TiO₂ substrate at 1,500 r.p.m. for 30 s and then annealed at 70 °C for 60 s. After the PbI₂ film cooled to room temperature, ammonium salt (90 mg FAI, 9 mg MACI, 6.39 mg MAI in 1 ml IPA) was spin coated on the PbI₂ film at 2,000 r.p.m. for 30 s and then annealed at 150 °C for 15 min. The addition of MACI can inhibit the transformation from black α -phase perovskite to yellow δ -phase non-perovskite, increasing the stability of the perovskite⁵¹. The characterization in the full text, and the champion PSCs, were fabricated via the two-step method.

Preparation of perovskite by the one-step method: the 1.86 M FA_{0.25}MA_{0.75}PbI₃ (DMF: DMSO, 13:2 volume/volume) precursor with 3% GBA was spin coated on the FTO/TiO₂ substrate at 4,000 r.p.m. for 18 s, and 200 μ l diethyl ether as an antisolvent was dripped on the centre of the film 12 s before the end of spin coating. Then the film was annealed at 110 °C for 10 min. The PSCs fabricated by the one-step method appear only in Supplementary Fig. 30.

Preparation of the o-F-PEAI layer: 10 mM o-F-PEAI dissolved in IPA was spin coated on the FTO/TiO₂/perovskite surface at 4,000 r.p.m. for 30 s without further annealing.

Preparation of the Spiro-OMeTAD hole transport layer: the Spiro-OMeTAD solution was prepared by mixing 72.3 mg Spiro-OMeTAD in 1 ml chlorobenzene with 26.6 μ l 4-tert-butylpyridine and 18 μ l lithium bis(trifluoromethanesulfonimide) (520 mg ml⁻¹ in acetonitrile); this was spin coated at 4,000 r.p.m. for 30 s.

Preparation of the Au electrode: Au electrode (60 nm) was deposited by thermal evaporation.

SEM, XRD and GIXRD measurements: surface morphology was characterized by cold field-emission scanning electron microscopy (SEM, Hitachi S-4800). The crystallinity of perovskite films was measured by X-ray diffraction (XRD, Bruker-D8-Discover) and grazing incidence X-ray diffraction (GIXRD, Micromax-007HF). The XRD using Cu K α (λ = 0.15406 nm) radiation (40 kV, 40 mA), the scan step was 0.01 s and the speed was 2° min⁻¹. The GIXRD pattern was collected using Mo K α (λ = 0.709 Å) with a sample-detector distance of 217 nm, and the grazing angle of incidence is 0.5°. The morphology evolution of the perovskite film under continuous water spray was observed under an optical microscope (OLYMPUS, DSX500). UV-vis measurement: the absorption intensity of perovskite films was measured by

UV-vis spectrophotometer (UV-2600). FTIR and XPS measurements: the chemical interaction of GBA with perovskite was characterized by Fourier transform infrared spectroscopy (FTIR, Bruker) in the region of 400–4,000 cm^{-1} . The surface chemical environment of the perovskite film was investigated with an X-ray photoelectron spectrometer (XPS, ESCALAB 250Xi). DLTS measurement: deep-level transient spectroscopy (DLTS, FT230) was used to characterize a wide variety of traps in the perovskite film. The sample structure is FTO/Perovskite/ MoO_x/Au . The temperature range is from 180 to 340 K. The bias voltage, pulse voltage and pulse width are -0.2 V, -0.01 V and 100 ms, respectively. Atomic force microscopy and KPFM measurements: atomic force microscopy (FMNanoview 1000) and Kelvin probe force microscopy (KPFM) were performed to characterize the surface morphology and surface potential of the control and target films. PL, PLQE, and TRPL measurements: steady-state photoluminescence (PL, FLS98003040404), photoluminescence quantum efficiency (PLQE) and time-resolved photoluminescence (TRPL) were used to characterize the carrier behaviour in the perovskite film. The excitation wavelength is 470 nm. PL mapping was carried out with laser confocal fluorescence lifetime imaging microscopy (Nikon-ARsIMP-LSM-Kit-Legend Elite-USX) at an excitation wavelength of 488 nm. The signal collection area is $55 \times 55 \mu\text{m}$. TRPL spectra can be fitted according to the following biexponential equation $I(t)$:

$$I(t) = A_1 \exp\left(-\frac{t}{\tau_1}\right) + A_2 \exp\left(-\frac{t}{\tau_2}\right)$$

where parameters A_1 and A_2 are the amplitude fraction for each decay component, τ_1 denotes the fast decay time constants corresponding to radiative recombination processes and τ_2 denotes the slow decay time constants corresponding to non-radiative recombination processes.

Density functional theory simulations

All spin-polarized density functional theory (DFT) calculations were performed using the Vienna Ab initio Simulation Package^{52,53}, with the generalized gradient approximation method for electronic exchange-correlation. Electron correlations were considered by the generalized gradient approximation method with the functional developed by Perdew, Burke and Ernzerhof^{52,54}. Core electrons were considered by the projector-augmented wave method^{55,56}. The cut-off was set to 500 eV and the van der Waals interactions were taken into consideration. The geometries of the models were considered fully relaxed when all the forces became lower than $0.05 \text{ eV } \text{\AA}^{-1}$. We constructed the $2 \times 2 \times 2 \alpha\text{-FAPbI}_3$ supercell from optimized M. T. Weller et al.⁵⁷ primitive cells for expansion. Therefore, the k-point mesh sampling of $3 \times 3 \times 3$ is used for structural optimization. The $\alpha\text{-FAPbI}_3$ structure parameters were listed in Supplementary Table 10. The binding energies (E_b) are calculated with: $E_b = E_{\text{AB}} - E_A - E_B$, where E_A , E_B , is the energy of the free A and B and E_{AB} is the total energy of the adsorption system. To study the effect of defects, the vacancy was created by randomly removing the species from the $\alpha\text{-FAPbI}_3$ supercell to calculate the defect formation energies of charged neutral defects⁵⁸.

Device performance measurement

The device efficiency was characterized by a Keithley 2400 source meter with a scan rate of 13 mV s^{-1} under simulated AM 1.5 G illumination (100 mW cm^{-2}) using a 150 W Class AAA solar simulator (XES-40SI, SAN-EI); the light intensity was calibrated by the National Institute of Metrology certified silicon solar cell. The external quantum efficiency and integrating current of perovskite solar cells were measured by QE-R systems (Enli Tech).

Device stability measurement

The devices used to test intrinsic stability were without encapsulation. For the long-term operational stability test, the devices were tracked

at the maximum power point under light-emitting diode (LED) illumination (AM 1.5 G, 100 mW cm^{-2}) at $50 \pm 5 \text{ }^\circ\text{C}$ in a N_2 glovebox. The LED light intensity was calibrated by the National Institute of Metrology certified silicon solar cell. For long-term ageing stability, the devices were stored in ambient air at room temperature ($25 \pm 5 \text{ }^\circ\text{C}$, 20% RH) and measured every two days.

The devices used to test extrinsic stability were encapsulated in the air using a glass cover and a UV-curable glue for edge sealing. For long-term operational stability, the devices were tracked at the MPP under LED illumination (AM 1.5 G, 100 mW cm^{-2}) at 85% RH in the environmental test box. The damp heat test was conducted by keeping the devices at $85 \text{ }^\circ\text{C}$, 85% RH in the climate test chamber. The accelerated degradation measurements of unencapsulated PSCs were conducted by keeping the devices at $25 \pm 5 \text{ }^\circ\text{C}$, 65% RH in the climate test chamber.

Reporting summary

Further information on research design is available in the Nature Portfolio Reporting Summary linked to this article.

Data availability

All data generated or analysed during this study are included in the published article and its Supplementary Information. Additional data are available from the corresponding author on reasonable request. Source data are provided with this paper.

References

- National Renewable Energy Laboratory *Best Research-Cell Efficiency Chart* (NREL, 2023); www.nrel.gov/pv/cell-efficiency.html
- Zhao, Y. et al. Inactive $(\text{PbI}_2)_2\text{RbCl}$ stabilizes perovskite films for efficient solar cells. *Science* **377**, 531–534 (2022).
- Bu, T. et al. Lead halide-templated crystallization of methylamine-free perovskite for efficient photovoltaic modules. *Science* **372**, 1327–1332 (2021).
- Hui, W. et al. Stabilizing black-phase formamidinium perovskite formation at room temperature and high humidity. *Science* **371**, 1359–1364 (2021).
- Li, N. et al. Liquid medium annealing for fabricating durable perovskite solar cells with improved reproducibility. *Science* **373**, 561–567 (2021).
- Lin, R. et al. All-perovskite tandem solar cells with improved grain surface passivation. *Nature* **603**, 73–78 (2022).
- Huang, H. et al. 24.8%-efficient planar perovskite solar cells via ligand-engineered TiO_2 deposition. *Joule* **6**, 2186–2202 (2022).
- Li, X. et al. Constructing heterojunctions by surface sulfidation for efficient inverted perovskite solar cells. *Science* **375**, 434–437 (2022).
- Cui, P. et al. Planar p–n homojunction perovskite solar cells with efficiency exceeding 21.3%. *Nat. Energy* **4**, 150–159 (2019).
- Yang, X. et al. Perovskite hetero-bilayer for efficient charge-transport-layer-free solar cells. *Joule* **6**, 1277–1289 (2022).
- Wang, Y. et al. Stabilizing heterostructures of soft perovskite semiconductors. *Science* **365**, 687–691 (2019).
- Min, H. et al. Perovskite solar cells with atomically coherent interlayers on SnO_2 electrodes. *Nature* **598**, 444–450 (2021).
- Yoo, J. et al. Efficient perovskite solar cells via improved carrier management. *Nature* **590**, 587–593 (2021).
- Jeong, J. et al. Pseudo-halide anion engineering for $\alpha\text{-FAPbI}_3$ perovskite solar cells. *Nature* **592**, 381–385 (2021).
- Caddeo, C. et al. Collective molecular mechanisms in the $\text{CH}_3\text{NH}_3\text{PbI}_3$ dissolution by liquid water. *ACS Nano* **11**, 9183–9190 (2017).
- Cheng, S. & Zhong, H. What happens when halide perovskites meet with water? *J. Phys. Chem. Lett.* **13**, 2281–229 (2022).

17. Tong, C. et al. Uncovering the veil of the degradation in perovskite $\text{CH}_3\text{NH}_3\text{PbI}_3$ upon humidity exposure: a first-principles study. *J. Phys. Chem. Lett.* **6**, 3289–3295 (2015).
18. Heo, S. et al. Origins of high performance and degradation in the mixed perovskite solar cells. *Adv. Mater.* **31**, 1805438 (2019).
19. Raval, P. et al. Understanding instability in formamidinium lead halide perovskites: kinetics of transformative reactions at grain and subgrain boundaries. *ACS Energy Lett.* **7**, 1534–1543 (2022).
20. Ho, K., Wei, M., Sargent, E. H. & Walker, G. C. Grain transformation and degradation mechanism of formamidinium and cesium lead iodide perovskite under humidity and light. *ACS Energy Lett.* **6**, 934–940 (2021).
21. Wang, X. et al. Tailoring component interaction for air-processed efficient and stable all-inorganic perovskite photovoltaic. *Angew. Chem. Int. Ed.* **59**, 13354–13361 (2020).
22. Xia, R. et al. An efficient approach to fabricate air-stable perovskite solar cells via addition of a self-polymerizing ionic liquid. *Adv. Mater.* **32**, 2003801 (2020).
23. Wang, J. et al. Ambient air processed highly oriented perovskite solar cells with efficiency exceeding 23% via amorphous intermediate. *Chem. Eng. J.* **446**, 136968 (2022).
24. Wang, M. et al. A universal strategy of intermolecular exchange to stabilize α -FAPbI₃ and manage crystal orientation for high-performance humid-air-processed perovskite solar cells. *Adv. Mater.* **34**, 2200041 (2022).
25. Wang, Z. et al. Achieving efficient and stable perovskite solar cells in ambient air through non-halide engineering. *Adv. Energy Mater.* **11**, 21021 (2021).
26. Salim, K. M. M. et al. Boosting long-term stability of pure formamidinium perovskite solar cells by ambient air additive assisted fabrication. *ACS Energy Lett.* **6**, 3511–3521 (2021).
27. Liu, Y. et al. Phase aggregation suppression of homogeneous perovskites processed in ambient condition toward efficient light-emitting diodes. *Adv. Funct. Mater.* **31**, 2103399 (2021).
28. Jung, K. et al. Ambient-air fabrication of stable mixed cation perovskite planar solar cells with efficiencies exceeding 22% using a synergistic mixed antisolvent with complementary properties. *Nano Energy* **89**, 106387 (2021).
29. Dai, X. et al. Efficient monolithic all-perovskite tandem solar modules with small cell-to-module derate. *Nat. Energy* **7**, 923–931 (2022).
30. Wang, G. et al. Thermal radiation driven ultrafast crystallization of perovskite films under heavy humidity for efficient inverted solar cells. *Adv. Mater.* **34**, 2205143 (2022).
31. Chao, L. et al. Direct and stable α -phase formation via ionic liquid solvation for formamidinium-based perovskite solar cell. *Joule* **6**, 2203–2217 (2022).
32. Wang, Z. et al. Air-processed MAPbBr₃ perovskite thin film with ultrastability and enhanced amplified spontaneous emission. *Small* **17**, 2101107 (2017).
33. Saidaminov, M. et al. Suppression of atomic vacancies via incorporation of isovalent small ions to increase the stability of halide perovskite solar cells in ambient air. *Nat. Energy* **3**, 648–654 (2018).
34. Aristidou, N. et al. Fast oxygen diffusion and iodide defects mediate oxygen-induced degradation of perovskite solar cells. *Nat. Commun.* **8**, 15218 (2017).
35. Lee, J. W. et al. Rethinking the A cation in halide perovskites. *Science* **375**, 835 (2022).
36. Tong, J. et al. Carrier lifetimes of >1 μs in Sn–Pb perovskites enable efficient all-perovskite tandem solar cells. *Science* **364**, 475–479 (2019).
37. Yang, S. et al. Tailoring passivation molecular structures for extremely small open-circuit voltage loss in perovskite solar cells. *J. Am. Chem. Soc.* **141**, 5781–5787 (2019).
38. Wang, R. et al. Constructive molecular configurations for surface-defect passivation of perovskite photovoltaics. *Science* **366**, 1509–1513 (2019).
39. Yang, X. et al. Multiple-defect management for efficient perovskite photovoltaics. *ACS Energy Lett.* **6**, 2404–2412 (2021).
40. Xue, J. et al. The surface of halide perovskites from nano to bulk. *Nat. Rev. Mater.* **5**, 809–827 (2020).
41. Chen, S. et al. Atomic-scale imaging of $\text{CH}_3\text{NH}_3\text{PbI}_3$ structure and its decomposition pathway. *Nat. Commun.* **12**, 5516 (2021).
42. Jodowski, A. et al. Large guanidinium cation mixed with methylammonium in lead iodide perovskites for 19% efficient solar cells. *Nat. Energy* **2**, 972–979 (2017).
43. Liang, Y. et al. Lead leakage preventable fullerene-porphyrin dyad for efficient and stable perovskite solar cells. *Adv. Funct. Mater.* **32**, 2110139 (2022).
44. Li, Z. et al. Organometallic-functionalized interfaces for highly efficient inverted perovskite solar cells. *Science* **376**, 416–420 (2022).
45. Wei, D. et al. Ion-migration inhibition by the cation- π interaction in perovskite materials for efficient and stable perovskite solar cells. *Adv. Mater.* **30**, 1707583 (2018).
46. Lin, D. et al. Ion migration accelerated reaction between oxygen and metal halide perovskites in light and its suppression by cesium incorporation. *Adv. Energy Mater.* **11**, 2002552 (2021).
47. Li, W. et al. The critical role of composition-dependent intragrain planar defects in the performance of $\text{MA}_{1-x}\text{FA}_x\text{PbI}_3$ perovskite solar cells. *Nat. Energy* **6**, 624–632 (2021).
48. Wang, F. et al. Defects engineering for high-performance perovskite solar cells. *npj Flexible Electron.* **2**, 22 (2018).
49. Khenkin, M. V. et al. Consensus statement for stability assessment and reporting for perovskite photovoltaics based on ISOS procedures. *Nat. Energy* **5**, 35–49 (2020).
50. Mendez, P. F. et al. Analysis of the UV-ozone-treated SnO_2 electron transporting layer in planar perovskite solar cells for high performance and reduced hysteresis. *Sol. RRL* **3**, 1900191 (2019).
51. Kim, M. et al. Methylammonium chloride induces intermediate phase stabilization for efficient perovskite solar cells. *Joule* **3**, 2179–2192 (2019).
52. Kresse, G. et al. Efficient iterative schemes for ab initio total-energy calculations using a plane-wave basis set. *Phys. Rev. B* **54**, 11169–11186 (1996).
53. Kresse, G. et al. Efficiency of ab-initio total energy calculations for metals and semiconductors using a plane-wave basis set. *Comput. Mater. Sci.* **6**, 15–50 (1996).
54. Perdew, J., Burke, K. & Ernzerhof, M. Generalized gradient approximation made simple. *Phys. Rev. Lett.* **77**, 3865–3868 (1996).
55. Blöchl, P. E. et al. Projector augmented-wave method. *Phys. Rev. B* **50**, 17953 (1994).
56. Kresse, G. et al. From ultrasoft pseudopotentials to the projector augmented-wave method. *Phys. Rev. B* **59**, 1758 (1999).
57. Weller, M. T., Weber, O. J., Frost, J. M. & Walsh, A. Cubic perovskite structure of black formamidinium lead iodide, α -[HC(NH₂)₂]PbI₃, at 298 K. *J. Phys. Chem. Lett.* **6**, 3209–3212 (2015).
58. Klimeš, J. et al. Van der Waals density functionals applied to solids. *Phys. Rev. B* **83**, 195131 (2011).

Acknowledgements

This work is supported partially by National Natural Science Foundation of China (grant numbers 52232008, 51972110, 52102245 and 52072121), Beijing Natural Science Foundation (2222076, 2222077), project of State Key Laboratory of Alternate Electrical

Power System with Renewable Energy Sources (LAPS202114), Huaneng Group Headquarters Science and Technology Project (HNKJ20-H88), the Fundamental Research Funds for the Central Universities (2020MS023, 2020MS028, 2023MS042) and the NCEPU 'Double First-Class' and sponsored by Beijing Nova Program. We thank H. Meng (National Institute of Metrology, China) for assistance with characterizing the performance of the device, C. Guo (Tsinghua University) and M. Chen (Peking University) for helping with the spectroscopy measurements. We also thank M. Wang, X. Ding and J. Chen (North China Electric Power University) for assisting with DFT calculation and discussion.

Author contributions

M.L. and L.Y. conceived the idea. M.L. and P.C. guided the work as supervisors. L.Y., H.H. and P.C. did experimental designs, device fabrication and data analysis. Z.L., S.D., Y.Y. and S.Q. participated in the device fabrications and some material and device characterizations. X.W., B.L., Q.Z., Y.L. and H.L. supported the measurement system construction, device fabrication, characterization and discussions. L.Y., H.H., P.C. and M.L. participated in manuscript writing and revising. X.Z., X.Y., J.J. and M.L. polished the manuscript language. All authors were involved in the discussions and approved the paper.

Competing interests

The authors declare no competing interests.

Additional information

Supplementary information The online version contains supplementary material available at <https://doi.org/10.1038/s41560-023-01358-w>.

Correspondence and requests for materials should be addressed to Meicheng Li.

Peer review information *Nature Energy* thanks Sofia Masi, Makhsud Saidaminov and the other, anonymous, reviewer(s) for their contribution to the peer review of this work.

Reprints and permissions information is available at www.nature.com/reprints.

Publisher's note Springer Nature remains neutral with regard to jurisdictional claims in published maps and institutional affiliations.

Springer Nature or its licensor (e.g. a society or other partner) holds exclusive rights to this article under a publishing agreement with the author(s) or other rightsholder(s); author self-archiving of the accepted manuscript version of this article is solely governed by the terms of such publishing agreement and applicable law.

© The Author(s), under exclusive licence to Springer Nature Limited 2023

Solar Cells Reporting Summary

Nature Research wishes to improve the reproducibility of the work that we publish. This form is intended for publication with all accepted papers reporting the characterization of photovoltaic devices and provides structure for consistency and transparency in reporting. Some list items might not apply to an individual manuscript, but all fields must be completed for clarity.

For further information on Nature Research policies, including our [data availability policy](#), see [Authors & Referees](#).

▶ Experimental design

Please check: are the following details reported in the manuscript?

1. Dimensions

- Area of the tested solar cells Yes No The aperture area is 0.08 cm² and 1 cm², which can be found in main text and supplementary information.
- Method used to determine the device area Yes No The area is determined by a mask with an opening area of 0.08 cm² and 1 cm².

2. Current-voltage characterization

- Current density-voltage (J-V) plots in both forward and backward direction Yes No We provide forward and backward scans in supplementary Fig. 25, 29 and 30.
- Voltage scan conditions Yes No The voltage scan conditions are forward (from -0.1 V to 1.2 V) and reverse (from 1.2 V to -0.1 V) scan with speed of 65 mV/s and dwell time of 5 ms, see method of device performance measurement.
For instance: scan direction, speed, dwell times
- Test environment Yes No The current-voltage characterization is performed in air at room temperature, see device performance measurement in method.
For instance: characterization temperature, in air or in glove box
- Protocol for preconditioning of the device before its characterization Yes No No preconditioning is required before characterization.
- Stability of the J-V characteristic Yes No See Fig.4e in main text and supplementary Fig. 25, 29 and 30.
Verified with time evolution of the maximum power point or with the photocurrent at maximum power point; see ref. 7 for details.

3. Hysteresis or any other unusual behaviour

- Description of the unusual behaviour observed during the characterization Yes No No unusual behaviour was observed and no significant hysteresis in supplementary Fig. 25, 29 and 30.
- Related experimental data Yes No We provide hysteresis scans in supplementary Fig. 25, 29 and 30.

4. Efficiency

- External quantum efficiency (EQE) or incident photons to current efficiency (IPCE) Yes No External quantum efficiency is shown in Fig.4b , supplementary Fig. 25, 29 and 30.
- A comparison between the integrated response under the standard reference spectrum and the response measure under the simulator Yes No The integrated short-circuit current from the EQE spectrum matches the short-circuit current from the J-V scan, see Fig.4b , supplementary Fig. 25, 29 and 30.
- For tandem solar cells, the bias illumination and bias voltage used for each subcell Yes No No tandem solar cells is fabricated in this work.

5. Calibration

- Light source and reference cell or sensor used for the characterization Yes No See device performance measurement in method.
- Confirmation that the reference cell was calibrated and certified Yes No See device performance measurement in method.

Calculation of spectral mismatch between the reference cell and the devices under test	<input type="checkbox"/> Yes <input checked="" type="checkbox"/> No	The light spectrum used for measurements matches well with the reference silicon cell, and we did not calculate the spectral mismatch between the reference cell and the tested devices.
6. Mask/aperture		
Size of the mask/aperture used during testing	<input checked="" type="checkbox"/> Yes <input type="checkbox"/> No	The size of the aperture area is 0.08 cm ² and 1 cm ² , which can be found in main text and supplementary information.
Variation of the measured short-circuit current density with the mask/aperture area	<input type="checkbox"/> Yes <input checked="" type="checkbox"/> No	The aperture area is fixed for each device.
7. Performance certification		
Identity of the independent certification laboratory that confirmed the photovoltaic performance	<input checked="" type="checkbox"/> Yes <input type="checkbox"/> No	The certificated PCE was obtained in the National Institute of Metrology, China (NIM, China), and the corresponding result is provided in the supplementary Fig. 27.
A copy of any certificate(s) <i>Provide in Supplementary Information</i>	<input checked="" type="checkbox"/> Yes <input type="checkbox"/> No	Supplementary Fig. 27.
8. Statistics		
Number of solar cells tested	<input checked="" type="checkbox"/> Yes <input type="checkbox"/> No	Histogram of the PCE value among 100 control PSCs and 100 target PSCs was shown in Fig. 4c and supplementary Fig. 26.
Statistical analysis of the device performance	<input checked="" type="checkbox"/> Yes <input type="checkbox"/> No	Statistical comparison of 100 PSCs was shown in supplementary Fig. 26. Plots of the box chart graphs containing the mean value, maximum/minimum values, and 25%-to-75%-region data of circuit current density, open-circuit voltage, fill factor, and power conversion efficiency.
9. Long-term stability analysis		
Type of analysis, bias conditions and environmental conditions <i>For instance: illumination type, temperature, atmosphere humidity, encapsulation method, preconditioning temperature</i>	<input checked="" type="checkbox"/> Yes <input type="checkbox"/> No	The long-term operational stability through MPP tracking of the unencapsulated PSCs under continuous AM1.5G (100 mW/cm ²) solar light in an N ₂ atmosphere at 50 ± 5°C (Fig. 4e). And the long-term stability of the unencapsulated PSCs in air was tested for up 2000 hours at 25 ± 5°C and 20% humidity (Fig. 4F). The long-term operational stability through MPP tracking of the encapsulated PSCs under continuous AM1.5G (100 mW/cm ²) solar light in ambient air at 85% RH (Fig. 4g). The damp heat tests (85°C and 85% RH) of encapsulated PSCs was shown in Fig. 4h. The accelerated degradation measurements of unencapsulated PSCs stored at 65% RH, was shown in Supplementary Fig. 31.